PAPER

Large energy-storage density in transition-metal oxide modified NaNbO$_3$−Bi(Mg$_{0.5}$Ti$_{0.5}$)O$_3$ lead-free ceramics through regulating the antiferroelectric phase structure†

Ao Tian, Ruzhong Zuo, [ID] * He Qi and Min Shi

Lead-free antiferroelectric (AFE) ceramics have attracted increasing attention in recent years for application in high-power capacitors owing to both environmental friendliness and high energy density. However, the relevant research progress has been seriously restricted by the limited amount of AFE candidate materials with low cost and excellent properties, which significantly rely on the AFE phase stability and crystal symmetry. In this work, NaNbO$_3$−Bi(Mg$_{0.5}$Ti$_{0.5}$)O$_3$ (NN−BMT) perovskite solid solutions were reported to obviously exhibit AFE phase structure dependent energy-storage performances, evolving from $W_{rec} \sim 1.08$ J cm^{-3} and $\eta \sim 19\%$ at $x = 0.05$ with an orthorhombic P phase (*Pbam*) under 25 kV mm^{-1} to 3.12 J cm^{-3} and 74%, respectively, at $x = 0.08$ with an orthorhombic R phase (*Pnma*) under 30 kV mm^{-1} owing to the transition of square-like double hysteresis loops into slim and double-like ones and the increased testable electric fields. Most interestingly, doping 0.5 mol% transition-metal oxides (CuO, CeO$_2$ and MnO$_2$) was found to evidently improve the sintering behaviour, bulk resistivity and defect structure, thus leading to largely enhanced dielectric breakdown strength. In particular, the MnO$_2$ doped 0.92NN−0.08BMT sample exhibits a large W_{rec} of ~ 5.57 J cm^{-3} and a high η of $\sim 71\%$ as well as excellent charge−discharge performance ($C_D = 636.7$ A cm^{-2}, $P_D = 63.7$ MW cm^{-3} and $t_{0.9} \sim 85$ ns), determined by means of the detailed analysis of the grain size distribution, impedance and X-ray photoelectron spectra. The results demonstrate that NN−BMT bulk ceramics could be very competitive lead-free AFE materials for energy-storage capacitors in pulsed power devices.

1. Introduction

Efficient storage of electrical energy is an increasingly important issue in the field of energy. Different from mechanical and electrochemical energy-storage methods, dielectric materials show great advantages in the pulsed power field owing to their high working voltage, large power density and superior charge–discharge rate. In particular, ceramic-based dielectric materials with thermal and chemical stability show huge potential for high-power energy-storage applications.[1–4] Generally, total energy-storage density W_{total}, recoverable energy-storage density W_{rec}, and energy-storage efficiency η can be calculated from the integral of polarization–electric field (P–E) hysteresis loops based on the following equations: $W_{total} = \int_0^{P_{max}} E dP$, $W_{rec} = \int_{P_r}^{P_{max}} E dP$ and $\eta = W_{rec}/W_{total} \times 100\%$, in which E, P,

P_{max} and P_r are the applied electric field, polarization under the applied electric field, the maximum polarization and the remanent polarization, respectively.[4] Obviously, large P_{max}, small P_r and high E are required to obtain desirable W_{rec} values from the above equations. Among various dielectrics materials, antiferroelectric materials (AFEs) show outstanding advantages owing to the electric field induced reversible AFE-ferroelectric (FE) phase transition corresponding to double P–E loops with large P_{max} and near-zero P_r.[5–7] In recent years, environment-friendly lead-free AFE materials have attracted increasing attention in the field of energy-storage capacitors.[8–13]

NaNbO$_3$ (NN) with a wide band gap shows an AFE orthorhombic P (*Pbma*) phase at room temperature and transforms into an AFE orthorhombic R (*Pnma*) phase at $T_{P-R} \sim 360$ °C.[14,15] Yet, an irreversible transformation of the AFE P phase in pure NN ceramic into an FE phase tends to accompany inferior energy-storage properties. The increase in the stability of the AFE P phase through the addition of some ABO$_3$ perovskites was found to produce repeatable square-like double P–E loops and thus improved energy-storage density.[16–19] However, an extremely low η value was usually obtained owing to obviously

Institute of Electro Ceramics & Devices, School of Materials Science and Engineering, Hefei University of Technology, Hefei, 230009, P. R. China. E-mail: piezolab@hfut. edu.cn

8352 | *J. Mater. Chem. A*, 2020, **8**, 8352–8359

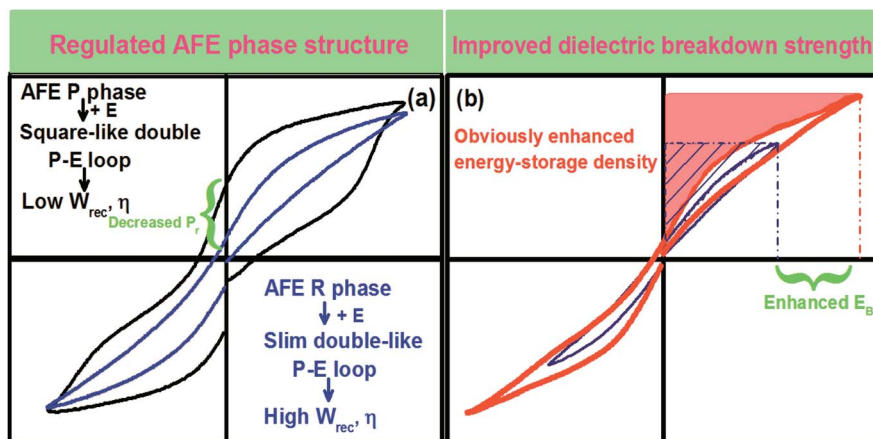This journal is © The Royal Society of Chemistry 2020

Fig. 1 Schematic diagram for the strategies of optimizing the energy-storage properties of NN–based AFE ceramics by means of (a) regulating the AFE phase structure and (b) improving the dielectric breakdown strength.

large polarization hysteresis during electric cycling. Compared with the AFE P phase, the AFE R phase, which can be stabilized at room temperature through further increasing the AFE phase stability,[10,11,20–23] generally exhibits not only a completely reversible AFE–FE phase transition, but also an obvious dielectric relaxation characteristic, both of which usually cause slim and double-like P–E loops. As a result, a highly enhanced driving field (E_{AF}) for the AFE to FE phase transition[10] and an obviously reduced hysteresis resulting from the rapid polarization response of anti-polar nanoregions[24] would be expected to be responsible for superior potentials in energy-storage capacitors. In practice, the electrical properties of ceramic-based capacitors strongly depend on the quality and microstructure of sintered samples. Except the improvement of the sintering process, some transition-metal oxides such as MnO_2 could also decrease the dielectric loss of ceramics by adjusting the state and content of charged defects, which are beneficial to enhance the dielectric breakdown strength and make full use of the energy-storage potential of materials. In a word, the strategies for the optimization of the energy-storage properties of NN–based AFE ceramics can be schematically depicted in Fig. 1, involving the regulation of the AFE phase structure and the increase of testable electric fields.

Bi(Mg$_{0.5}$Ti$_{0.5}$)O$_3$ (BMT) is an orthorhombic complex perovskite at room temperature with a low tolerance factor ($\tau = 0.94$) and probably antiferroelectric due to the antiparallel shifts of Bi^{3+} and antiphase tilting of oxygen octahedra,[25] which is anticipated to help stabilize the AFE phase structure of NN ceramics, considering the lowering of the AFE P to R phase transition temperature.[26] In this work, NN–BMT AFE solid solution ceramics with a higher amount of BMT were synthesized *via* a solid-state reaction method in order to explore the relationship between AFE phase structural evolution and energy-storage properties. In combination with the optimization of dielectric breakdown properties by doping some transition-metal oxides, an ultrahigh $W_{rec} \sim 5.57$ J cm^{-3} and a desirable $\eta \sim 71\%$ were obtained in 0.5 mol% MnO_2 doped 0.92NN–0.08BMT bulk ceramics.

2.   Experimental section

The $(1 - x)$NN–xBMT ceramics ($0 \leq x \leq 0.08$) were prepared by a conventional solid-state reaction method. Na$_2$CO$_3$, Nb$_2$O$_5$, Bi$_2$O$_3$, (MgCO$_3$)$_4$·Mg(OH)$_2$·5H$_2$O and TiO$_2$ with 99.9% purity were weighed as starting materials according to their chemical formula, and then mixed thoroughly in ethanol with zirconia balls for 4 h. After drying, well-mixed powders were calcined at 850 °C for 4 h in air. The calcined powders were ball-milled again for 8 h together with 0.7 wt% polyvinyl butyral (PVB) as a binder and 0.5 mol% MnO$_2$, CuO or CeO$_2$ as a dopant ($(1 - x)$ NN–xBMT–Mn/Cu/Ce). After compaction, the samples were sintered at 1190–1260 °C for 2 h in air. After being sintered, disks were polished to a thickness of ~0.2 mm, and silver electrodes were painted on the two main surfaces (round electrode with a radius of 1 mm) and fired at 550 °C for 30 min for P–E and dielectric breakdown strength tests.

The phase structure of the sintered ceramics was determined by using a powder X-ray diffractometer (XRD, D/Max-RB, Rigaku, Tokyo, Japan) with Cu Kα radiation. Rietveld refinements on the full XRD patterns were performed by using the program GSAS to identify the crystal symmetry and structural parameters. The valence states of Ti, O and Mn in MnO$_2$ doped 0.92NN–0.08BMT sample powders were determined by means of X-ray photoelectron spectroscopy (XPS, ESCALAB250Li, Thermo Scientific, USA) using an Al-Kα ($h = 1486.6$ eV) X-ray source, in which binding energies were referenced to the C 1s line at 284.8 eV from adventitious carbon. The powders were dried in a vacuum for 24 h before the XPS test to avoid the influence of the adsorbed H$_2$O. The sample density was estimated by the Archimedes method. The grain morphology was observed on a field-emission scanning electron microscope (FE-SEM, JEM-2100F, JEOL, Japan). Before observation, the disks were polished and thermally etched at 980–1040 °C for 10 min. Dielectric property measurements and impedance spectroscopy were performed by using an LCR meter (Agilent E4980A, Santa Clara, CA) during heating. The P–E hysteresis loops were measured by using a ferroelectric test system (Precision

Multiferroic; Radiant Technologies Inc, Albuquerque, New Mexico) at 10 HZ. The dielectric breakdown strength (E_B) was measured using a voltage breakdown test device (BDJC-50 kV, Beijing Jingyi Instrument Equipment Co. Ltd., Beijing, China) at room temperature and the samples were prepared under the same processes as the P–E test samples to ensure the consistency of the results. The energy release performances were measured *via* a commercial charge–discharge platform (CFD-001, Gogo Instruments Technology, Shanghai, China) with a certain RLC load circuit and a sample size of 0.2 mm (thickness) $\times$ 9.6 mm^2 (electrode area).

3. Results and discussion

Fig. 2(a) shows the temperature and frequency dependent dielectric permittivity of $(1 - x)$NN–xBMT ceramics as indicated. There is an obvious dielectric anomaly peak at 200 °C in the $x = 0.05$ composition, corresponding to the phase transition temperature $T_{P–R}$ from an AFE P phase to an AFE R phase in NN-based ceramics.[11,27] It is about 360 °C for pure NN ceramics and decreases with increasing BMT content till it cannot be detected above room temperature in the $x = 0.07$ and 0.08 compositions.[26] Meanwhile, the room-temperature dielectric permittivity significantly increases when x exceeds 0.05 and then declines with further increasing x, as can be seen in the inset of Fig. 2(a). For the $x = 0.06$ sample, the P–R phase transition peak can still be observed above room temperature; however, its room-temperature dielectric permittivity is much higher than that of the $x = 0.05$ sample, indicating that the $x = 0.06$ sample at room temperature is dominated by the relaxor AFE R phase, in addition to a small amount of AFE P phase as a result of the

thermal hysteresis of the P–R transition during heating.[11] As $x > 0.06$, the disappearance of the P–R dielectric anomaly peak and the large room-temperature dielectric permittivity together indicate that the samples at room temperature should be solely composed of the AFE R phase. In order to refine the crystal structure of each composition, the Rietveld refinement results for sintered $(1 - x)$NN–xBMT ceramic powders at room temperature are given in Fig. 2(b–e) and Table S1.† It can be seen that the crystal structure of the samples transforms from a pure P phase at $x = 0.05$ to a coexisting P and R phase at $x = 0.06$ and finally to a pure R phase in $x = 0.07$ and $x = 0.08$ ceramics, in good agreement with the analysis result in Fig. 2(a). The above results indicate that the addition of BMT with a low tolerance factor can effectively enhance the stability of the AFE phase in NN.

Accompanying the composition induced phase transition, an obvious change in the P–E and J–E curves can be found, as shown in Fig. 3(a) and (b). Although the pure NN ($x = 0$) exhibits an irreversible field induced AFE–FE phase transition, as shown in Fig. S1,† the $x = 0.05$ and $x = 0.06$ samples exhibit reversible square-like double P–E loops with large polarization hysteresis, corresponding to low E_{AF} values and high P_r values. As a result, poor energy-storage performances were obtained in these AFE P phase compositions, as indicted in Fig. 3(c). As x increases from 0.05 and 0.06 to 0.07 and 0.08, double square P–E loops gradually transform into slim loops with near-zero P_r. These slim double-like loops were formed owing to obviously enhanced dielectric relaxation characteristics of the AFE R phase, which causes a rapid polarization response and significantly increased phase transition field.[10] As a result, obviously improved energy-storage properties of large $W_{rec} \sim 2.81$ J cm^{-3} and 2.49 J cm^{-3} and desirable $\eta \sim 81\%$ and $\sim 85\%$ were obtained in $x = 0.07$ and 0.08 ceramics at 25 kV mm^{-1}, respectively, as shown in Fig. 3(c), exhibiting obvious advantages of the AFE R phase over the AFE P phase. Fig. 3(d) shows P–E loops for $x = 0.07$ and 0.08 samples
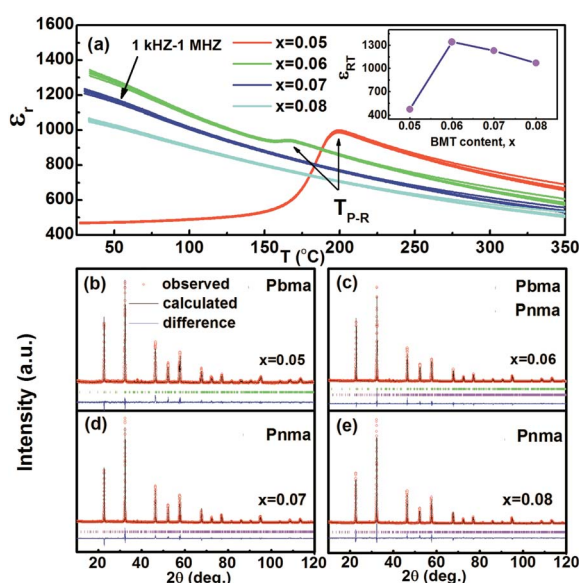

Fig. 2 (a) The dielectric permittivity (ε_r) as a function of temperature and frequency for $(1 - x)$NN–xBMT ceramics with $x = 0.05$, $x = 0.06$, $x = 0.07$ and $x = 0.08$, and the Rietveld refinement results of XRD patterns for $(1 - x)$NN–xBMT ceramics with (b) $x = 0.05$, (c) $x = 0.06$, (d) $x = 0.07$ and (e) $x = 0.08$. The inset of (a) shows the variation of room-temperature permittivity (ε_{RT}) with the BMT content.
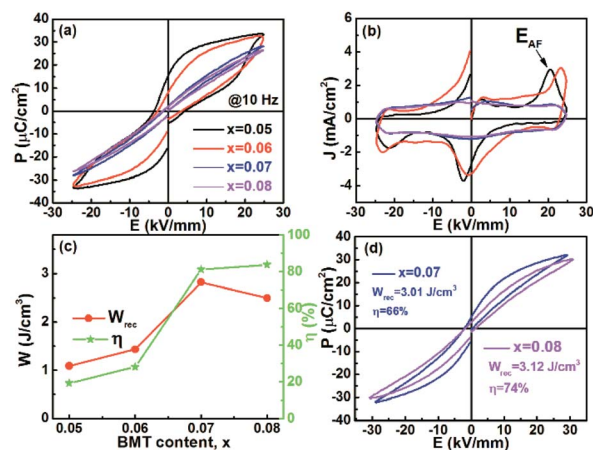

Fig. 3 (a) P–E hysteresis loops for $(1 - x)$NN–xBMT ceramics under 25 kV mm^{-1}, (b) the corresponding polarization current *versus* electric field (J–E) curves, (c) W_{rec} and η changing with the BMT content and (d) P–E hysteresis loops for $x = 0.07$ and 0.08 samples under their maximum testable electric fields.

8354 | *J. Mater. Chem. A*, 2020, **8**, 8352–8359

This journal is © The Royal Society of Chemistry 2020

under their maximum testable electric fields. Even though the $x = 0.08$ sample exhibits a smaller P_{max} than the $x = 0.07$ sample, a slightly larger testable electric field can be applied on the $x = 0.08$ ceramic owing to the smaller dielectric permittivity. As a result, both relatively large W_{rec} and η values of $W_{rec} \sim 3.12$ J cm^{-3} and $\eta \sim 74\%$ were obtained in the $x = 0.08$ sample. Generally, the dielectric loss mainly transforms into heat, which would enhance the risk of thermal breakdown in practical applications.[28] Therefore, the simultaneous achievement of larger W_{rec} and η values would make the capacitors advantageous for future pulsed power applications.

In order to further optimize the energy-storage properties, the $x = 0.08$ composition was doped with 0.5 mol% MnO$_2$, CuO or CeO$_2$. Fig. 4(a–c) indicate the variation of dielectric permittivity as a function of temperature for different oxide doped $x = 0.08$ samples measured during heating. It can be seen that the addition of oxide additives has only a slight influence on the dielectric permittivity and loss of all three samples, particularly for room-temperature ε_r and tan δ values. Moreover, the credible E_B value of undoped and doped samples can be evaluated by using the following Weibull distribution functions:[29]

$$X_i = \ln(E_i) \qquad (1)$$

$$Y_i = \ln(\ln(1/(1 - P_i))) \qquad (2)$$

$$P_i = i/(n + 1) \qquad (3)$$

where E_i is the measured breakdown electric field of the ith samples in the ascending order arrangement ($E_1 < E_2 \ldots < E_n$), P_i is the probability of dielectric breakdown, n is the total number of the test samples, and X_i and Y_i are two Weibull expression variables. The Weibull data points and the fitting lines for different samples are shown in Fig. 4(d). All the studied samples display a linear relationship with the Weibull modulus m (the slope of the lines) over 7, indicating the good reliability of the analysis results. As shown in Fig. 4(e), the E_B value of the $x = 0.08$ sample can be obviously improved by doping oxide
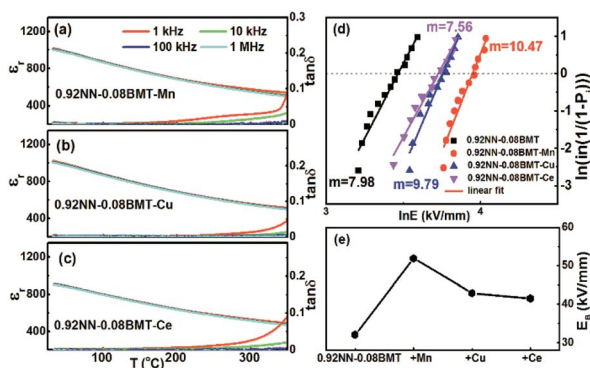
additives; in particular, the 0.5 mol% MnO$_2$ doped sample exhibits the optimal dielectric breakdown properties.

The energy-storage performance of the 0.92NN–0.08BMT–Mn ceramic was evaluated considering the improvement of the E_B value, as shown in Fig. 5. Fig. 5(a) presents P–E loops measured under different electric fields at room temperature. It is obvious that P_{max} increases monotonously with increasing electric field up to 48 kV mm^{-1}, while low-hysteresis double-like P–E loops with $P_r \sim 0$ μC cm^{-2} can be detected in the studied electric field range, thus generating an ultrahigh W_{rec} of ~ 5.57 J cm^{-3} and a desirable η of $\sim 71\%$. Moreover, the pulsed charge–discharge properties were measured to evaluate the actual energy-storage performances of practical capacitor applications. Fig. 6(a) shows the underdamped discharge current–time (I–t) curves for the 0.92NN–0.08BMT–Mn ceramic under different electric fields at room temperature. It can be found that all curves display a similar discharge period of ~30 ns under different electric fields, suggesting stable discharge capability. The corresponding maximum current (I_{max}), current density ($C_D = I_{max}/S$) and power density ($P_D = E \times I_{max}/2S$) as a function of the electric field are revealed in Fig. 6(b). It can be found that I_{max}, C_D and P_D can linearly increase with increasing electric field. The I_{max} value increases from 29.5 A at 8 kV mm^{-1} to 61.3 A at 20 kV mm^{-1}, while the values of C_D and P_D reach a maximum of 636.7 A cm^{-2} and 63.7 MW cm^{-3} at 20 kV mm^{-1}, respectively. Fig. 6(c) shows the over-damped pulsed discharge electric current time (I–t) curves, which can be used to calculate the discharge energy density (W_D) under different electric fields using the following equation:

$$W_D = R \int I(t)^2 dt / V \qquad (4)$$

where R is the load resistor (100 Ω) and V is the sample volume. I_{max} and W_D values vary from 6.9 A and 0.21 J cm^{-3} to 18.7 A and 1.17 J cm^{-3}, respectively, as the electric field increases from

Fig. 4 (a–c) The dielectric permittivity (ε_r) and loss (tan δ) as a function of temperature and frequency for 0.92NN–0.08BMT ceramics doped with different oxides (MnO$_2$, CuO and CeO$_2$, respectively); (d) the Weibull distribution and linear-fit lines of the E_B values and (e) the corresponding E_B values of the 0.92NN–0.08BMT sample undoped and doped with different oxides.

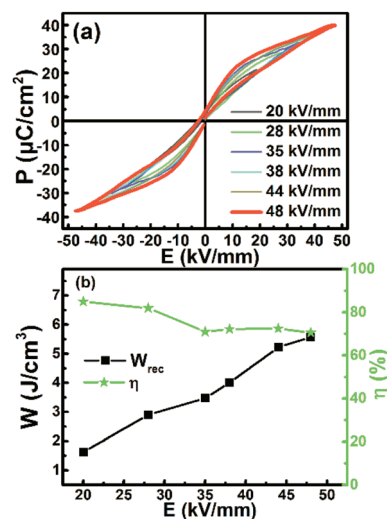
Fig. 5 (a) Bipolar P–E loops under different electric fields and (b) the corresponding energy-storage properties of the 0.92NN–0.08BMT–Mn sample.
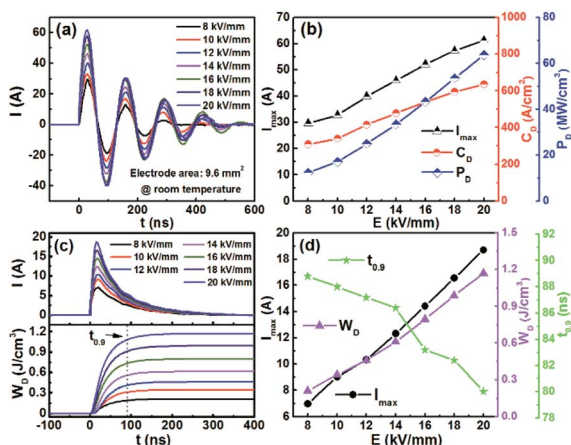
This journal is © The Royal Society of Chemistry 2020

J. Mater. Chem. A, 2020, 8, 8352–8359 | 8355

Fig. 6 (a) Underdamped discharge waveforms and (b) I_{max}, C_D and P_D for the 0.92NN–0.08BMT–Mn sample under different electric fields, (c) overdamped discharge curves and calculated discharge energy density W_D as a function of time for the 0.92NN–0.08BMT–Mn sample at a fixed load resistance of 100 Ω under different electric fields and (d) the corresponding I_{max}, W_D and $t_{0.9}$ values for the 0.92NN–0.08BMT–Mn sample under different electric fields.

8 kV mm^{-1} to 20 kV mm^{-1}. The $t_{0.9}$ value represents the time required for releasing 90% stored energy. A small $t_{0.9}$ of 80–89 ns can be obtained under different electric fields, suggesting a fast discharge rate. $t_{0.9}$ together with I_{max} and W_D under different electric fields is summarized in Fig. 6(d). A comparison of the energy-storage and charge–discharge performances between this work and several recently reported ceramics in Table 1[5,30–35] demonstrates that the 0.92NN–0.08BMT–Mn ceramic has competing energy-storage performances.

According to the above analysis results, it is essential to explore the mechanism of improved energy-storage properties for oxide doped $x = 0.08$ samples. Fig. 7 shows the SEM photos on well-polished and thermally etched surfaces of different samples sintered at their optimum temperatures. It is worth noting that the optimum sintering temperature of all doped samples was reduced to different degrees, compared with that of the undoped AFE sample, ranging from 1240 °C for the $x = 0.08$ sample to 1190 °C, 1210 °C and 1210 °C for the MnO$_2$, CuO and CeO$_2$ doped samples, respectively. Under respective optimal sintering conditions, each sample exhibits a dense and

homogeneous microstructure with a high relative density of 96%. In addition, the average grain size (G_a) significantly decreases from 2.05 μm (0.92NN–0.08BMT) to 0.76 μm (0.92NN–0.08BMT–Mn), 0.97 μm (0.92NN–0.08BMT–Cu) and 0.88 μm (0.92NN–0.08BMT–Ce). It is well known that the decreased grain size would contribute to the increase of the E_B value by an exponential decay relationship, $E_B \propto (G_a)^{-a}$.[36] Among the oxide doped $x = 0.08$ samples, the MnO$_2$ doped ceramic has the lowest sintering temperature and the smallest grain size, probably indicating the most efficient improvement of the dielectric breakdown behaviour. Furthermore, impedance spectroscopy was performed from 380 to 520 °C and in the frequency range of 20 Hz to 2 MHz. The Z'–Z'' curves for different samples obtained at 500 °C are shown in Fig. 8(a), where Z' and Z'' represent the real and imaginary parts of impedance, respectively. A parallel R∥CPE equivalent circuit model was used for the impedance analysis. It can be seen that the Z'–Z'' plots of all samples exhibit nearly a single semicircle at 500 °C, indicating that the grain boundary plays a dominant role in the whole conduction. This should be related to the high resistivity of the grain boundary. Larger Z' values are usually related to higher voltage endurance capability, indicating the improvement of insulating properties after doping these transition-metal oxides, particularly for the MnO$_2$ doped sample.

According to the Arrhenius equation, the activation energy (E_a) of the conductivity can be calculated from the slope of ln σ − 1000/T plots:[37]

$$\sigma = \sigma_0 \exp(E_a/k_B T) \quad (5)$$

where σ is the bulk conductivity, σ_0 is the pre-exponent constant, E_a is the activation energy of conduction and k is the Boltzmann constant. As shown in Fig. 8(b) and S2,† the calculated E_a values of different samples are in the range of 1.32–1.94 eV, indicating that the conduction mechanism in the measured ceramics should be attributed to the migration of double ionized oxygen vacancies.[38] Compared with the matrix sample, the E_a value increases after doping oxides, meaning the movement of electric charges becomes harder in doped samples. During sintering, oxygen vacancies can be formed because of sodium volatilization at high temperatures. After doping, the generation of oxygen vacancies in the 0.92NN–

Table 1 Comparison of the energy-storage and charge–discharge performances between the 0.92NN–0.08BMT–Mn ceramic and several recently reported ceramics

| Composition	W_{rec} (J cm^{-3})	η (%)	E (kV mm^{-1})	C_D (A cm^{-2})	P_D (MW cm^{-3})	$t_{0.9}$ (ns)	Ref.
Pb$_{0.94}$La$_{0.04}$[(Zr$_{0.70}$Sn$_{0.30}$)$_{0.90}$Ti$_{0.10}$]O$_3$	1.39	92	10.4	820	43	400	5
0.90BaTiO$_3$–0.10(Bi$_{0.9}$Na$_{0.1}$)(In$_{0.8}$Zr$_{0.2}$)O$_3$	1.33	88	18	796	39.8	190	30
0.88BaTiO$_3$–0.12Bi(Li$_{0.5}$Nb$_{0.5}$)O$_3$	2.03	88	27	—	—	150	31
0.54BiFeO$_3$–0.34BaTiO$_3$–0.12(Sr$_{0.7}$Bi$_{0.2}$)TiO$_3$	1.74	74	15	1184.7	59.2	125	32
0.85NaNbO$_3$–0.15Bi(Mg$_{2/3}$Nb$_{1/3}$)NbO$_3$	2.40	90	30	370	18	—	33
0.93NaNbO$_3$–0.07Bi(Mg$_{0.5}$Zr$_{0.5}$)O$_3$	2.31	80.2	25.5	—	—	—	34
0.94(0.65Bi$_{0.5}$Na$_{0.5}$TiO$_3$–0.35Bi$_{0.1}$Sr$_{0.85}$TiO$_3$) –0.06(K$_{0.5}$Na$_{0.5}$NbO$_3$)	2.65	84.6	18	—	—	1010	35
0.92NN–0.08BMT–Mn	5.57	71	48	636.7	63.7	85	This work
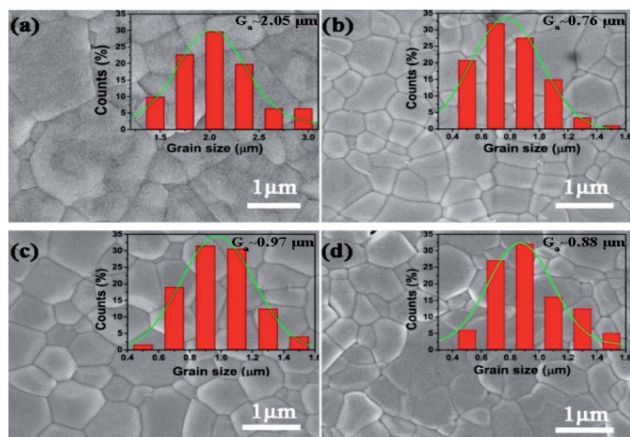
Fig. 7 SEM micrographs on the polished and thermally etched surfaces of (a) 0.92NN–0.08BMT, (b) 0.92NN–0.08BMT–Mn, (c) 0.92NN–0.08BMT–Cu and (d) 0.92NN–0.08BMT–Ce ceramic samples sintered at their respective optimum temperatures. The inset of each figure corresponds to the statistical analysis of grain size distribution of each sample.

0.08BMT ceramic would be suppressed due to the notably decreased sintering temperature. Moreover, the trapping effect of defect dipoles also contributes to the enhancement of E_a values. Taking the CuO doped sample as an example, an oxygen

vacancy ($V_O^{\cdot\cdot}$) is formed when B-site Nb^{5+} is substituted by Cu^{2+}. $V_O^{\cdot\cdot}$ would further turn into defect dipoles ($Cu_{Nb}''' - V_O^{\cdot\cdot}$) with dopant ions. The conduction of $V_O^{\cdot\cdot}$ would be blocked by charged defect dipoles, making the long-range migration of oxygen vacancies harder in the bulk sample.[39] A similar phenomenon also exists in the MnO_2 or CeO_2 doped 0.92NN–0.08BMT samples. Different from CuO and CeO_2, MnO_2 shows different valences at various temperatures during sintering. In order to clarify the reason for the good insulating properties of the 0.92NN–0.08BMT–Mn ceramic, high-resolution XPS spectra of Ti 2p and O 1s for the 0.92NN–0.08BMT sample (sintered at 1240 °C), the 0.92NN–0.08BMT–Mn sample (sintered at 1190 °C), the 0.92NN–0.08BMT–Cu and 0.92NN–0.08BMT–Ce samples (sintered at 1210 °C) were recorded, as shown in Fig. 8(c, d) and S3.† The chemical states of Ti and O were fitted to quantitatively analyze different valence states. As shown in Fig. 8(c), the peak located at lower binding energy is attributed to Ti^{3+}, while the peak located at higher binding energy is attributed to Ti^{4+}. In the O 1s region, the two peaks are attributed to the lattice oxygen (O_L, on the lower binding energy side) and oxygen vacancies (O_H, on the higher binding energy side). The area of each region (filled with different colors) represents the relative content of the corresponding valence. After the addition of MnO_2, the areas of Ti^{3+} and O_H were found to reduce obviously, indicating enhanced Ti^{4+} stability and decreased oxygen vacancy defects. And the lowest O_H content can be found
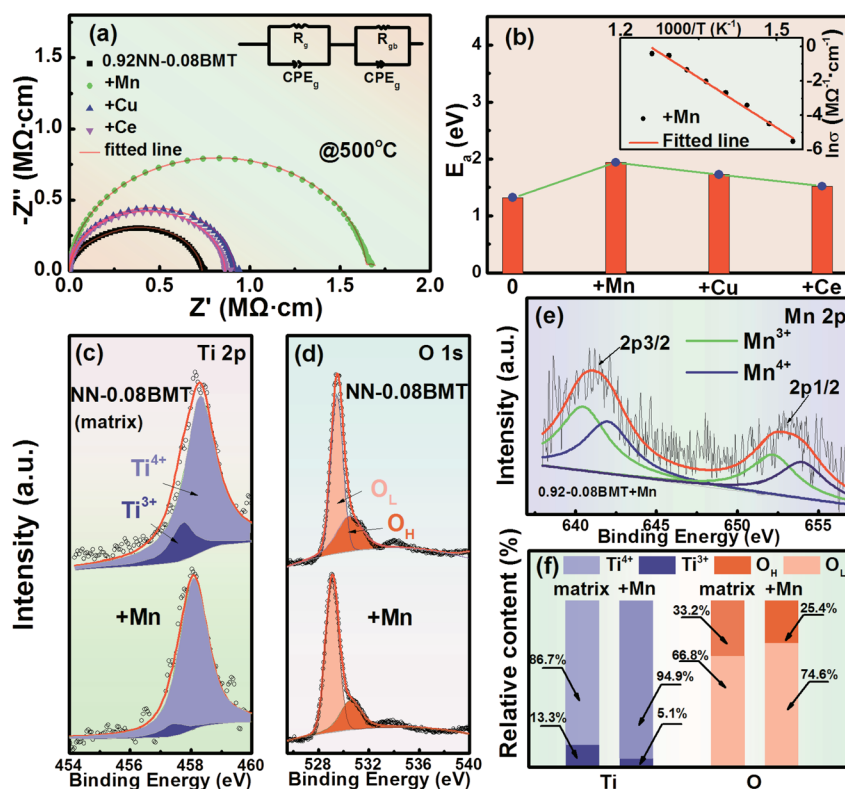

Fig. 8 (a) The measured and fitted complex impedance data for 0.92NN–0.08BMT ceramics doped with different oxides at 500 °C; (b) the E_a value for 0.92NN–0.08BMT ceramics doped with different oxides. The inset of (b) shows the Arrhenius plot of the ac conductivity; XPS data of (c) Ti 2p and (d) O 1s for the 0.92NN–0.08BMT and 0.92NN–0.08BMT–Mn samples, respectively; (e) the XPS Mn 2p line of the 0.92NN–0.08BMT–Mn sample; (f) the relative content of Ti^{3+}, Ti^{4+}, O_L, and O_H for the 0.92NN–0.08BMT and the 0.92NN–0.08BMT–Mn samples.

This journal is © The Royal Society of Chemistry 2020

J. Mater. Chem. A, 2020, 8, 8352–8359 | 8357

in the 0.92NN–0.08BMT–Mn sample among the different oxide doped compositions, as shown in Fig. 8(d) and S3.† Fig. 8(e) represents the XPS narrow scans of Mn 2p for the 0.92NN–0.08BMT–Mn sample, in which the overlapped Mn $2p_{3/2}$ and $2p_{1/2}$ peaks were fitted to analyze the valence states of the doped Mn ions. The Mn $2p_{3/2}$ peaks can be only fitted with two peaks, one at 640.43 eV, and the other at 641.98 eV, corresponding to Mn^{3+} and Mn^{4+}, respectively.[40] The variation of the valence state of Mn ions should be ascribed to the transformation from Mn^{4+} into Mn^{3+} when the sintering temperature is higher than 1020 °C,[41] helping prevent the transformation of $Ti^{4+} \rightarrow Ti^{3+}$ and reduce the oxygen vacancy concentration. The relative contents of ions with different valences for the 0.92NN–0.08BMT matrix and the MnO_2 doped samples are summarized in Fig. 8(f). As a result, significantly decreased relative contents of Ti^{3+} and O_H were found after the addition of MnO_2, which is responsible for the enhancement of E_a and E_B values. Among these three different oxide additives, MnO_2 exhibits the most efficient improvement, leading to a significantly reduced grain size, increased bulk resistivity and desired chemical inhibition effect on reducing oxygen vacancy concentration. As a result, the outstanding dielectric breakdown strength and energy-storage performance can be obtained in the 0.92NN–0.08BMT–Mn AFE ceramic.

4.   Conclusions

In summary, $(1 - x)$NN–xBMT lead-free solid solution ceramics were found to exhibit an obvious phase transformation from an AFE orthorhombic P phase (*Pbma*) to an AFE orthorhombic R phase (*Pnma*) with increasing BMT content, accompanying significantly enhanced energy-storage properties as a result of enhanced AFE phase stability and improved reversibility of the AFE–FE phase transition. The optimum energy-storage properties of $W_{rec} \sim 2.49$ J cm^{-3} and $\eta \sim 85\%$ were obtained in the $x = 0.08$ sample with an AFE R phase structure under 25 kV mm^{-1}. In addition, obviously improved E_B values were achieved by doping three different oxide additives, among which MnO_2 proves to be the most efficient owing to the reduced grain size, increased bulk resistivity and desired chemical inhibition effect. As a result, an ultrahigh W_{rec} of ~ 5.57 J cm^{-3} and a large η of $\sim 71\%$ as well as an excellent charge–discharge performance ($C_D = 636.7$ A cm^{-2}, $P_D = 63.7$ MW cm^{-3} and $t_{0.9} \sim 85$ ns) were achieved in the 0.92NN–0.08BMT–Mn bulk ceramic under 48 kV mm^{-1}. Furthermore, the mechanism for the improved dielectric breakdown properties by doping transition-metal oxides was explored by means of the analysis of grain size distribution, impedance spectra and XPS data. The results obtained in this work suggest that NN–BMT lead-free AFE solid solution ceramics could be potential candidate dielectrics for the application of energy-storage capacitors in the field of pulsed power electronics.

Conflicts of interest

There are no conflicts to declare.

Acknowledgements

References

1 Z. H. Yao, Z. Song, H. Hao, Z. Y. Yu, M. H. Cao, S. J. Zhang, M. T. Lanagan and H. X. Liu, *Adv. Mater.*, 2017, **29**, 1601727.
2 Z. Liu, T. Lu, J. M. Ye, G. S. Wang, X. L. Dong, R. Withers and Y. Liu, *Adv. Mater. Technol.*, 2018, 1800111.
3 D. W. Wang, G. Wang, S. Murakami, Z. M. Fan, A. Feteira, D. Zhou, S. K. Sun, Q. L. Zhao and I. M. Reaney, *J. Adv. Dielectr.*, 2018, **8**, 1830004.
4 L. T. Yang, X. Kong, F. Li, H. Hao, Z. X. Cheng, H. X. Liu, J. F. Li and S. J. Zhang, *Prog. Mater. Sci.*, 2019, **102**, 72–108.
5 R. Xu, B. R. Li, J. J. Tian, Z. Xu, Y. J. Feng, X. Y. Wei, D. Huang and L. J. Yang, *Appl. Phys. Lett.*, 2017, **110**, 142904.
6 X. H. Hao, *J. Adv. Dielectr.*, 2013, **3**, 1330001.
7 H. S. Wang, Y. C. Liu, T. Q. Yang and S. J. Zhang, *Adv. Funct. Mater.*, 2018, 1807321.
8 L. Zhao, Q. Liu, J. Gao, S. J. Zhang and J. F. Li, *Adv. Mater.*, 2017, **29**, 1701824.
9 Y. Tian, L. Jin, Q. Y. Hu, K. Yu, Y. Y. Zhang, G. Viola, I. Abrahams, Z. Xu, X. Y. Wei and H. X. Yan, *J. Mater. Chem. A*, 2019, **7**, 834–842.
10 H. Qi, R. Z. Zuo, A. W. Xie, A. Tian, J. Fu, Y. Zhang and S. J. Zhang, *Adv. Funct. Mater.*, 2019, 1903877.
11 A. W. Xie, H. Qi, R. Z. Zuo, A. Tian, J. Chen and S. J. Zhang, *J. Mater. Chem. C*, 2019, **7**, 15153–15161.
12 J. L. Li, F. Li, Z. Xu and S. J. Zhang, *Adv. Mater.*, 2018, 1802155.
13 L. Zhang, Y. P. Pu, M. Chen and G. Liu, *J. Eur. Ceram. Soc.*, 2018, **38**, 5388–5395.
14 A. M. Glazer and H. D. Megaw, *Acta Crystallogr., Sect. A: Cryst. Phys., Diffr., Theor. Gen. Crystallogr.*, 1973, **29**, 489–495.
15 Y. I. Yuzyuk, P. Simon, E. Gagarina, L. Hennet, D. Thiaudière, V. I. Torgashev, S. I. Raevskaya, I. P. Raevskii, L. A. Reznitchenko and J. L. Sauvajol, *J. Phys.: Condens. Matter*, 2005, **17**, 4977–4990.
16 H. Shimizu, H. Z. Guo, S. E. Reyes-Lillo, Y. Mizuno, K. M. Rabe and C. A. Randall, *Dalton Trans.*, 2015, **44**, 10763–10772.
17 H. Qi, R. Z. Zuo, A. W. Xie, J. Fu and D. Zhang, *J. Eur. Ceram. Soc.*, 2019, **39**, 3703–3709.
18 Z. Y. Liu, J. S. Lu, Y. Q. Mao, P. R. Ren and H. Q. Fan, *J. Eur. Ceram. Soc.*, 2018, **38**, 4939–4945.
19 J. M. Ye, G. S. Wang, X. F. Chen, F. Cao and X. L. Dong, *Appl. Phys. Lett.*, 2019, **114**, 122901.
20 M. X. Zhou, R. H. Liang, Z. Y. Zhou and X. L. Dong, *J. Mater. Chem. A*, 2018, **6**, 17896–17904.
21 Y. Z. Fan, Z. Y. Zhou, R. H. Liang and X. L. Dong, *J. Eur. Ceram. Soc.*, 2019, **39**, 4770–4777.
22 Z. T. Yang, H. L. Du, L. Jin, Q. Y. Hu, H. Wang, Y. F. Li, J. F. Wang, F. Gao and S. B. Qu, *J. Mater. Chem. A*, 2019, **7**, 27256–27266.

8358 | *J. Mater. Chem. A*, 2020, **8**, 8352–8359

This journal is © The Royal Society of Chemistry 2020

23 J. P. Shi, X. L. Chen, X. Li, J. Sun, C. C. Sun, F. H. Pang and H. F. Zhou, *J. Mater. Chem. C*, 2020, **8**, 3784–3794.

24 H. Qi and R. Z. Zuo, *J. Mater. Chem. A*, 2020, **8**, 2369–2375.

25 D. D. Khalyavin, A. N. Salak, N. P. Vyshatko, A. B. Lopes, N. M. Olekhnovich, A. V. Pushkarev, I. I. Maroz and Y. V. Radyush, *Chem. Mater.*, 2006, **18**, 5104–5110.

26 R. Y. Jing, L. Jin, Y. Tian, Y. Y. Huang, Y. Lan, J. Xu, Q. Y. Hu, H. L. Du, X. Y. Wei, D. Guo, J. H. Gao and F. Gao, *Ceram. Int.*, 2019, **45**, 21175–21182.

27 S. K. Mishra, N. Choudhury, S. L. Chaplot, P. S. R. Krishna and R. Mittal, *Phys. Rev. B: Condens. Matter Mater. Phys.*, 2007, **76**, 024110.

28 S. Ray, *An introduction to high voltage engineering*, Prentice-Hall of India Pvt., 2013.

29 W. Weibull, *J. Appl. Mech.*, 1951, **18**, 293–297.

30 F. Li, M. X. Zhou, J. W. Zhai, B. Shen and H. R. Zeng, *J. Eur. Ceram. Soc.*, 2018, **38**, 4646–4652.

31 W. B. Li, D. Zhou, L. X. Pang, R. Xu and H. H. Guo, *J. Mater. Chem. A*, 2017, **5**(37), 19607–19612.

32 F. Li, J. W. Zhai, B. Shen, H. R. Zeng, X. D. Jian and S. G. Lu, *J. Alloys Compd.*, 2019, **803**, 185–192.

33 J. M. Ye, G. S. Wang, M. X. Zhou, N. T. Liu, X. F. Chen, S. Li, F. Cao and X. L. Dong, *J. Mater. Chem. C*, 2019, **7**, 5639–5645.

34 N. Qu, H. L. Du and X. H. Hao, *J. Mater. Chem. C*, 2019, **7**, 7993–8002.

35 Z. B. Pan, D. Hu, Y. Zhang, J. J. Liu, B. Shen and J. W. Zhai, *J. Mater. Chem. C*, 2019, **7**, 4072–4078.

36 T. Tunkasiri and G. Rujijanagul, *J. Mater. Sci. Lett.*, 1996, **15**, 1767–1769.

37 J. J. Huang, Y. Zhang, T. Ma, H. T. Li and L. W. Zhang, *Appl. Phys. Lett.*, 2010, **96**, 042902.

38 R. Moos and K. H. Härdtl, *J. Appl. Phys.*, 1996, **80**, 393–400.

39 N. Masó and A. R. West, *Chem. Mater.*, 2012, **24**, 2127–2132.

40 C. D. Wagner and G. E. Mullenberg, *Handbook of X-ray Photoelectron Spectroscopy*, Perkin-Elmer, Eden Prairie, Minnesota, 1979.

41 G. R. Li, L. Y. Zheng, Q. R. Yin, B. Jiang and W. W. Cao, *J. Appl. Phys.*, 2005, **98**, 064108.

This journal is © The Royal Society of Chemistry 2020

J. Mater. Chem. A, 2020, **8**, 8352–8359 | **8359**